Prospects for γ-ray observations of narrow-line Seyfert 1 galaxies with the Cherenkov Telescope Array – II. γ–γ absorption in the broad-line region radiation fields

P. Romano, M. Böttcher, L. Foschini, C. Boisson, S. Vercellone, M. Landoni

▶ To cite this version:

P. Romano, M. Böttcher, L. Foschini, C. Boisson, S. Vercellone, et al.. Prospects for γ-ray observations of narrow-line Seyfert 1 galaxies with the Cherenkov Telescope Array – II. γ–γ absorption in the broad-line region radiation fields. Monthly Notices of the Royal Astronomical Society, 2020, 494 (1), pp.411-424. 10.1093/mnras/staa600 . hal-02507758

HAL Id: hal-02507758
https://hal.science/hal-02507758

Submitted on 21 Jun 2022

HAL is a multi-disciplinary open access archive for the deposit and dissemination of scientific research documents, whether they are published or not. The documents may come from teaching and research institutions in France or abroad, or from public or private research centers.

L'archive ouverte pluridisciplinaire **HAL**, est destinée au dépôt et à la diffusion de documents scientifiques de niveau recherche, publiés ou non, émanant des établissements d'enseignement et de recherche français ou étrangers, des laboratoires publics ou privés.

Monthly Notices
of the
ROYAL ASTRONOMICAL SOCIETY

MNRAS **494,** 411–424 (2020)
Advance Access publication 2020 March 3

doi:10.1093/mnras/staa600

Prospects for γ-ray observations of narrow-line Seyfert 1 galaxies with the Cherenkov Telescope Array – II. γ–γ absorption in the broad-line region radiation fields

P. Romano,[1,2★†] M. Böttcher,[3] L. Foschini,[1] C. Boisson,[2] S. Vercellone[1] and M. Landoni[1]

[1] *INAF, Osservatorio Astronomico di Brera, Via E. Bianchi 46, I-23807 Merate, Italy*
[2] *LUTH, Observatoire de Paris, CNRS, Université Paris Diderot, PSL Research University Paris, 5 place Jules Janssen, F-92195 Meudon, France*
[3] *Centre for Space Research, North-West University, Potchefstroom 2531, South Africa*

Accepted 2020 February 25. Received 2020 February 18; in original form 2020 January 14

ABSTRACT

Gamma-ray emitting narrow-line Seyfert 1 (γ-NLS1) galaxies possibly harbour relatively low-mass black holes (10^6–10^8 M$_\odot$) accreting close to the Eddington limit, and share many characteristics with their sibling sources, flat-spectrum radio quasars. Although they have been detected in the MeV–GeV band with *Fermi*–LAT, they have never been seen in the very high energy band with current imaging atmospheric Cherenkov telescopes (IACTs). Thus, they are key targets for the next-generation IACT, the Cherenkov Telescope Array (CTA). In a previous work we selected, by means of extensive simulations, the best candidates for a prospective CTA detection (SBS 0846+513, PMN J0948+0022, and PKS 1502+036) taking into account the effects of both the intrinsic absorption (approximated with a cut-off at 30 GeV), and the extragalactic background light on the propagation of γ-rays. In this work, we simulate the spectra of these three sources by adopting more realistic broad-line region (BLR) absorption models. In particular, we consider the detailed treatment of γ–γ absorption in the radiation fields of the BLR as a function of the location of the γ-ray emission region with parameters inferred from observational constraints. We find that, due to the energy range extent and its sensitivity, CTA is particularly well suited to locate the γ-ray emitting region in γ-NLS1. In particular CTA will be able not only to distinguish whether the γ-ray emitting region is located inside or outside the BLR, but also where inside the BLR it may be.

Key words: galaxies: jets – galaxies: Seyfert – gamma rays: galaxies – galaxies: individual: SBS 0846+513 – galaxies: individual: PMN J0948+0022 – galaxies: individual: PKS 1502+036.

1 INTRODUCTION

Narrow-line Seyfert 1 galaxies (NLS1s) are a subclass of active galactic nuclei (AGN) whose optical properties, with narrow permitted emission lines (H β FWHM < 2000 km s^{-1}, Goodrich 1989), weak forbidden [O III] lines ([O III] λ5007/H $\beta < 3$), and strong iron emission lines (high Fe II/ H β, Osterbrock & Pogge 1985), set them apart from the more general population of Seyfert 1 galaxies (broad-line Seyfert 1 s, BLS1s). These characteristics (e.g. Peterson et al. 2004) are generally explained in terms of lower masses (10^6–10^8 M$_\odot$) of the central black hole when compared to BLS1s with similar luminosities, and higher accretion rates, close to the Eddington limit (but see, also, Viswanath et al. 2019 and references therein). Recent evidence has been found that a small fraction (4–7 per cent, Komossa et al. 2006; Cracco et al. 2016) of NLS1s are radio loud and show a flat radio spectrum (Oshlack, Webster & Whiting 2001; Zhou et al. 2003; Yuan et al. 2008; see also, Lähteenmäki et al. 2017). Further evidence of a hard component in some of their X-ray spectra and spectral variability in the hard X-ray was also found (Foschini et al. 2009).

Following the first detection of an NLS1 in γ-rays ($E > 100$ MeV) by *Fermi*-LAT (PMN J0948+0022, Abdo et al. 2009a, b; Foschini et al. 2010) a new subclass of NLS1s was defined, the γ-ray emitting NLS1 (γ-NLS1) galaxies, now consisting of about 20 objects, as sources whose overall observational properties are strongly reminiscent of those of jetted sources (see e.g. Foschini 2012; Foschini et al.

★ E-mail: patrizia.romano@inaf.it
† Visiting Astronomer at LUTH.

© 2020 The Author(s)
Published by Oxford University Press on behalf of the Royal Astronomical Society

Downloaded from https://academic.oup.com/mnras/article/494/1/411/5775321 by CNRS - ISTO user on 21 June 2022

Table 1. Sample of γ-NLS1, and the parameters of their γ-ray spectra in several flux states, optically derived luminosities, adopted for the simulations.

Source name	State	RA (deg)	Decl (deg)	z	K_0 (ph cm^{-2} MeV^{-1} s^{-1})	E_0 (MeV)	Γ	Ref.	$L^a_{\mathrm{H}\beta}$	L^b_{disc}
SBS 0846+513	High	132.51	51.14	0.585	1.08×10^{-10}	300	2.10	1	1.32	3.94
PMN J0948+0022	High	147.24	0.37	0.585	9.60×10^{-10}	300	2.55	2	3.73	11.8
	‘Flare’	–	–	–	2.88×10^{-9}	300	2.55	3	–	–
PKS 1502+036	High	226.26	3.44	0.408	1.4×10^{-9}	250	2.54	4	0.41	1.12

Notes. Redshift are drawn from NED. Luminosities estimated from optical (SDSS) data, as drawn from Foschini et al. (2015).
[a] H β luminosities in units of 10^{42} erg s^{-1}.
[b] Disc luminosities in units of 10^{44} erg s^{-1}.
References. For the PL models we adopted:
(1) Paliya et al. (2016);
(2) Foschini et al. (2011);
(3) See Romano et al. (2018): flaring state, assumed a factor of 3 brighter than the high state;
(4) D’Ammando et al. (2016b).

Table 2. BLR properties adopted for the γ–γ absorption grids (Section 3).

Source name	L^a_{BLR} (erg s^{-1})	R^b_{BLR} (cm)	u^c_{BLR} (erg cm^{-3})	r^b_1 (cm)	R^b_{in} (cm)	R^b_{out} (cm)	r^b_5 (cm)
SBS 0846+513	2.8	1.87	2.12×10^{-3}	203	1.69	2.06	0.19
PMN J0948+0022	7.91	3.26	1.98×10^{-3}	351	2.93	3.58	0.33
PKS 1502+036	0.869	1.00	2.29×10^{-3}	108	0.90	1.10	0.10

[a] Luminosities in units of $\times\, 10^{43}$ erg s^{-1}.
[b] Radii in units of $\times\, 10^{17}$ cm.
[c] u in units of $\times\, 10^{-3}$ erg cm^{-3}.

2015; D’Ammando et al. 2016a). Currently, however, no detection has been obtained in the very high energy (VHE, $E > 50$ GeV) regime (Whipple upper limit (UL) on 1H 0323+342, Falcone et al. 2004; VERITAS UL on PMN J0948+0022, D’Ammando et al. 2015a; H.E.S.S. UL on PKS 2004−447, H.E.S.S. Collaboration 2014).

In Romano et al. (2018) (Paper I), we considered the prospects for observations of γ-NLS1 as a class of sources to investigate with the Cherenkov Telescope Array (CTA) since the detection in the VHE regime would provide important clues on the location of the γ-ray emitting region. The CTA, as the next-generation ground-based γ-ray observatory, will boast a wide energy range (20 GeV to 300 TeV) which will be achieved by including three classes of telescopes with different sizes, i.e. the large-sized telescopes (LSTs, diameter $D \sim 23$ m), the medium-sized telescopes (MSTs, $D \sim 12$ m) and the small-sized telescopes (SSTs, primary mirror $D \sim 4$ m). CTA will also provide all-sky coverage, by consisting of two separate arrays on two sites, one in each hemisphere. The current CTA set-up (Hofmann 2017a, b) includes a Northern site at the Observatorio del Roque de los Muchachos on the island of La Palma (Spain) where 4 LSTs and 15 MSTs, covering an area of $\sim$1 km^2, will be located, and a Southern site at the European Southern Observatory’s (ESO’s) Paranal Observatory in the Atacama Desert (Chile), that will cover an area of about 4 km^2, where 4 LSTs, 25 MSTs, and 70 SSTs will be located.

The extensive set of simulations of all currently known γ-ray emitters identified as NLS1s (20 sources) reported in Romano et al. (2018) took into account the effect of both the extragalactic background light on the propagation of γ-rays and intrinsic absorption components. These latter components, mainly due to the currently unconstrained location of the γ-ray emitting region, were approximated analytically with a cut-off at 30 GeV ($\propto e^{-E/E_{\mathrm{cut}}}$, $E_{\mathrm{cut}} = 30$ GeV). In this work, we consider the only three sources that were deemed good candidates for a prospective CTA detection in Romano et al. (2018), SBS 0846+513, PMN J0948+0022, and PKS 1502+036, and simulate their spectra by adopting more realistic broad-line region (BLR) absorption models. In particular, we shall consider the detailed treatment of γ–γ absorption in the radiation fields of the BLR of these NLS1s as a function of the location of the γ-ray emission region as proposed by Böttcher & Els (2016).

In Section 2, we detail our sample; in Section 3, we describe the BLR internal absorption modelling, in Section 4, we describe our simulation set-up. In Section 5, we present our results and in Section 6 discuss their implications.

2 DATA SAMPLE

Of the 20-source sample described in Romano et al. (2018, table 1), as expected due to the faintness of γ-NLS1s, we only consider SBS 0846+513, PMN J0948+0022, and PKS 1502+036, which were deemed good candidates for a prospective CTA detection and, hence, should afford the chance to extract meaningful spectra. For those three sources different activity states were defined/studied in Paper I whose properties are recalled below. The properties of these sources are found in Table 1, and include coordinates (Equatorial, J2000, Cols. 3, 4), redshift (Col. 5), the spectral parameters for the best-fitting models to the *Fermi* data adopted for each source and flux state (Cols. 6–9), where the spectra are described as a power-law (PL)

$$\frac{\mathrm{d}N}{\mathrm{d}E} = K_0 \left(\frac{E}{E_0}\right)^{-\Gamma}, \qquad (1)$$

Downloaded from https://academic.oup.com/mnras/article/494/1/411/5775321 by CNRS - ISTO user on 21 June 2022

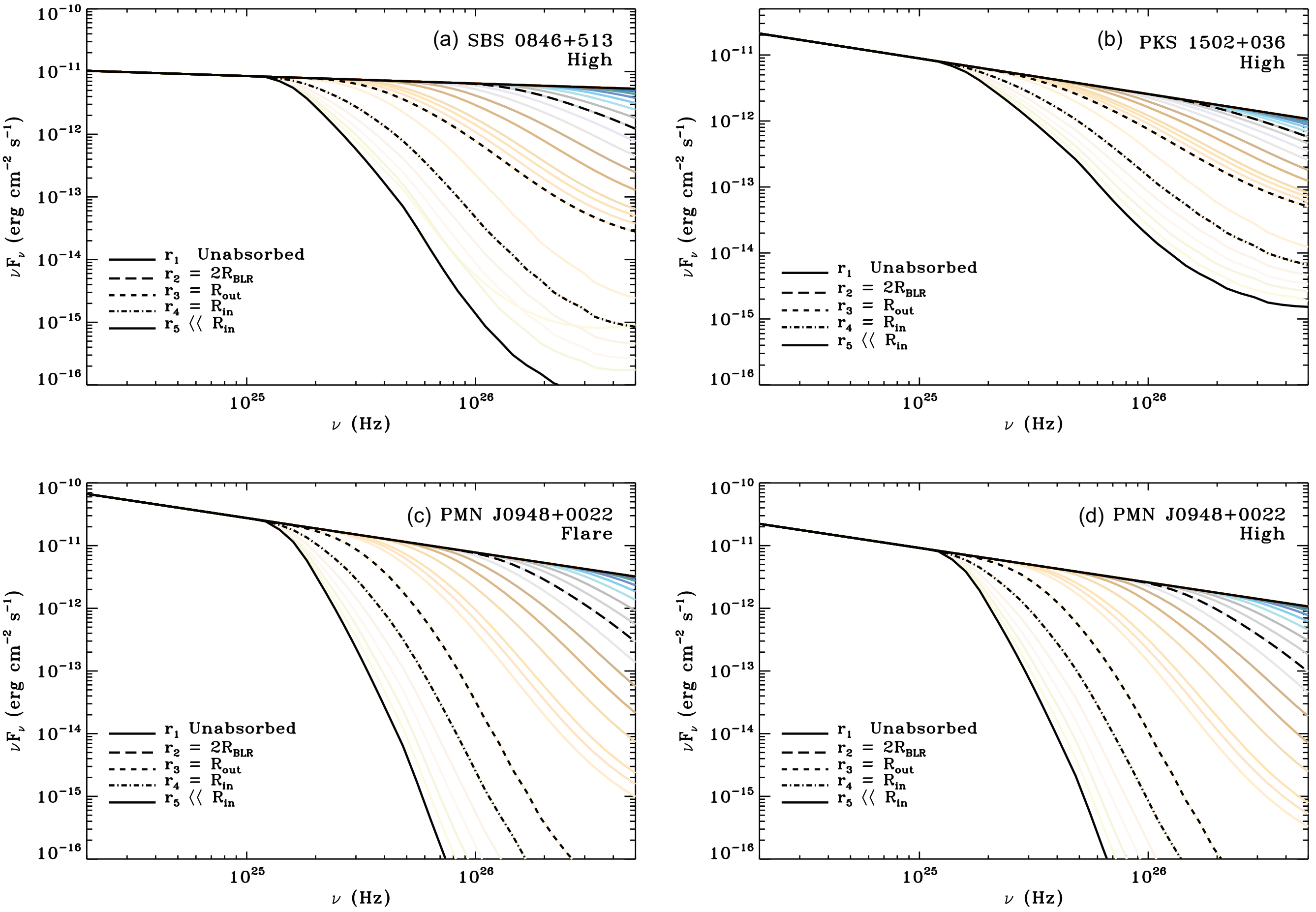

Figure 1. Input models including only the BLR contribution to absorption (no EBL is taken into account). The grid is calculated for a range of distances, from $R_{\rm em} \ll R_{\rm in}$ to $R_{\rm em} \gg R_{\rm out}$. The models in black are five exemplary cases, from least absorbed to most absorbed: $r_1 \gg R_{\rm BLR}$, $r_2 = 2\,R_{\rm BLR}$, $r_3 = R_{\rm out}$, $r_4 = R_{\rm in}$, and $r_5 \ll R_{\rm in}$, while the coloured lines represent models with intermediate radii. A colour version is available online.

where K_0 is the normalization (in units of ph cm^{-2} s^{-1} MeV^{-1}), E_0 is the pivot energy (in MeV), and Γ is the PL photon index. Table 1 also reports the Hβ and disc luminosities derived from Table 2 of Foschini et al. (2015), that we adopted as the basis of the modelling of the BLR absorption we present in Section 3. In the following we summarise the models we considered for the three sources.

For SBS 0846+513 we considered only the high-flux state, which was derived from Paliya et al. (2016) and was modelled by means of a simple PL model with photon index 2.10 ± 0.05 and an integrated γ-ray flux ($0.1 < E < 300$ GeV) of $(9.92 \pm 0.84) \times 10^{-8}$ ph cm^{-2} s^{-1} (F2 flare, integrated over 120 days).

For PMN J0948+0022 two flux states were considered. The high state ($F_{\rm E\,>\,100 MeV} = (1.02 \pm 0.02) \times 10^{-6}$ ph cm^{-2} s^{-1}) is described by a simple PL model with photon index $\Gamma = 2.55 \pm 0.02$ (Foschini et al. 2011). We also defined a 'flare' state as three times brighter than the high state, 3 h long, with the same spectral shape which could represent a very bright state for this source and an excellent case to test the specific CTA capabilities in detecting bright short transients.

For PKS 1502+036 only the high-flux state was considered, as derived from D'Ammando et al. (2016b, 1 d integration) and described by a PL with a photon index $\Gamma = (2.54 \pm 0.04)$ and a flux $F_{0.1\,<\,E\,<\,300\rm GeV} = (93 \pm 19) \times 10^{-8}$ ph cm^{-2} s^{-1}.

3 BLR INTERNAL ABSORPTION MODELLING

For each source and each flux state, we produced a grid of models accounting for γ–γ absorption in the BLR as a function of the location of the γ-ray emission region. We followed the methods described in Böttcher & Els (2016), but with fixed BLR radius and luminosity derived from observational constraints as detailed below.

In Böttcher & Els (2016), the BLR is represented as a spherical, homogeneous shell with inner and outer boundaries $R_{\rm in}$ and $R_{\rm out}$, respectively, and the γ-ray emission region is located at a distance $R_{\rm em}$ from the central supermassive black hole of the AGN. For this work, we assumed that the BLR extends from $R_{\rm in} = 0.9\,R_{\rm BLR}$ to $R_{\rm out} = 1.1\,R_{\rm BLR}$. For a given (measured) accretion-disc luminosity, $L_{\rm disc} = 10^{45}\,L_{\rm disc,45}$ erg s^{-1}, the radius of the BLR is estimated as (Bentz et al. 2013),

$$R_{\rm BLR} = 3 \times 10^{17} L_{\rm disc,45}^{1/2} \quad ({\rm cm}). \tag{2}$$

The BLR luminosity $L_{\rm BLR}$ is calculated by using the measured luminosity of the Hβ emission line according to the relationship

$$L_{\rm BLR} = 21.2\,L_{\rm H\beta} \quad ({\rm erg\,s^{-1}}). \tag{3}$$

The model BLR spectrum used for the BLR γ–γ absorption calculation includes the 21 strongest emission lines with relative luminosities taken from the quasar spectrum template by Francis et al. (1991). For the purpose of our γ–γ opacity estimates, the

Downloaded from https://academic.oup.com/mnras/article/494/1/411/5775321 by CNRS - ISTO user on 21 June 2022

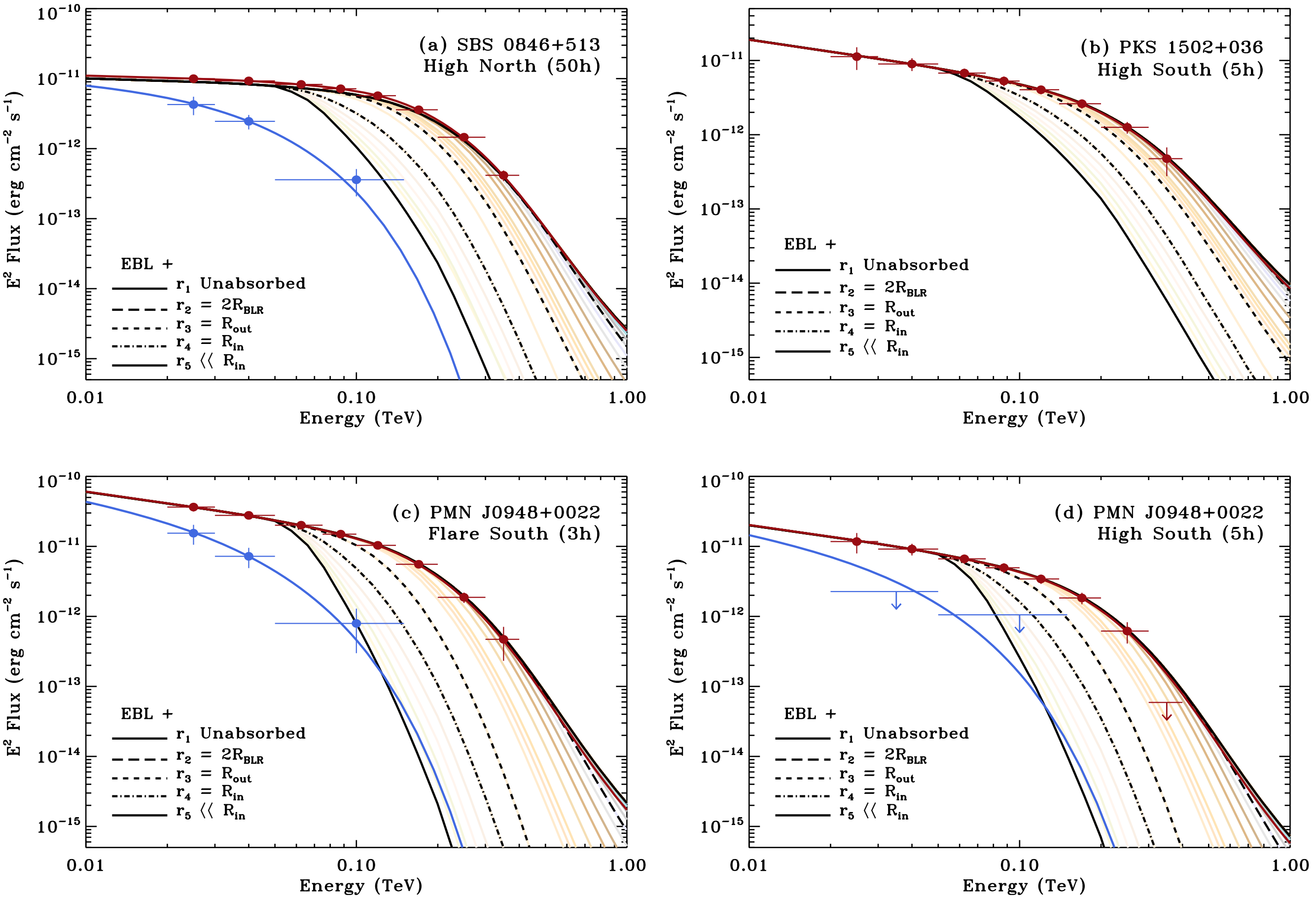

Figure 2. Input models including both the BLR and the EBL contribution to absorption with the same colour scheme as Fig. 1. Overplotted are also the input models (blue and red lines) and results (blue and red points) of Romano et al. (2018, table 1, figs 8, 9, 11, and 12): the blue lines refer to the PL model affected by both EBL and BLR absorption, (a cut-off at 30 GeV, with the exception of the high state of PKS 1502+036), while the red lines refer to models only affected by EBL, that is, assuming that the blue spectra extend unbroken above 20–30 GeV. A colour version is available online.

Table 3. Setup of the (`ctools`) simulations: site, IRF, and exposure time.

Source name (State)	Site^a	IRF	Exp. (h)
SBS 0846+513 (High)	N	`North_z20_N_50h`	50
PMN J0948+0022 (Flare)	S	`South_z20_average_5h`	3
PMN J0948+0022 (High)	S	`South_z20_average_5h`	5
PKS 1502+036 (High)	S	`South_z20_average_5h`	5

^{a}CTA site selected for the simulations: N = North (La Palma, latitude: 28.76 N), S = South (Paranal, latitude: 24.68 S).

stratification of the BLR (with different emission lines originating at different radii within the BLR) is not taken into account. For a detailed treatment of the effects of such stratification on the BLR γ–γ opacity, see the appendix of Finke (2016). The BLR radiation energy density at $R \ll R_{\rm in}$ is derived from the BLR radius and luminosity (equations 2 and 3),

$$u_{\rm BLR} = \frac{L_{\rm BLR}}{4\pi R_{\rm BLR}^2 c} \quad ({\rm erg\,cm^{-3}}). \tag{4}$$

A summary of the parameters for the BLR of each source is reported in Table 2. Grids of models are calculated for a range of distances, from $R_{\rm em} \ll R_{\rm in}$ to $R_{\rm em} \gg R_{\rm out}$. In Fig. 1, we display the grid of models for each source. Among those, we selected five exemplary cases, from least absorbed to most absorbed:

(i) $r_1 \gg R_{\rm BLR}$,
(ii) $r_2 = 2\,R_{\rm BLR}$,
(iii) $r_3 = R_{\rm out}$,
(iv) $r_4 = R_{\rm in}$,
(v) $r_5 \ll R_{\rm in}$.

Finally, in Fig. 2 we show the spectral energy distributions (SEDs) inputs to our simulations, including both the BLR contribution to absorption and the attenuation due to the extragalactic background light (EBL, calculated by adopting the model of Domínguez et al. 2011). Fig. 2 also shows, as a comparison with previous work, the models simulated in Romano et al. (2018). The blue lines refer to the PL models affected by both EBL and BLR absorption, the latter modelled as a cut-off at 30 GeV, with the exception of the high state of PKS 1502+036.[1] The red lines refer to models only affected by EBL (no BLR contribution), assuming that the blue spectra can extend unbroken above 20–30 GeV. All points are the results of the simulations in Romano et al. (2018, figs 8, 9, 11, and 12).

---

[1] In Romano et al. (2018) it was assumed that, as also concluded by D'Ammando et al. (2016b), due to the 3-week delay observed between the γ and radio (15 GHz) light-curve peaks, the dissipation region may lie outside the BLR, hence no cut-off was applied to mimic the BLR absorption.

Downloaded from https://academic.oup.com/mnras/article/494/1/411/5775321 by CNRS - ISTO user on 21 June 2022

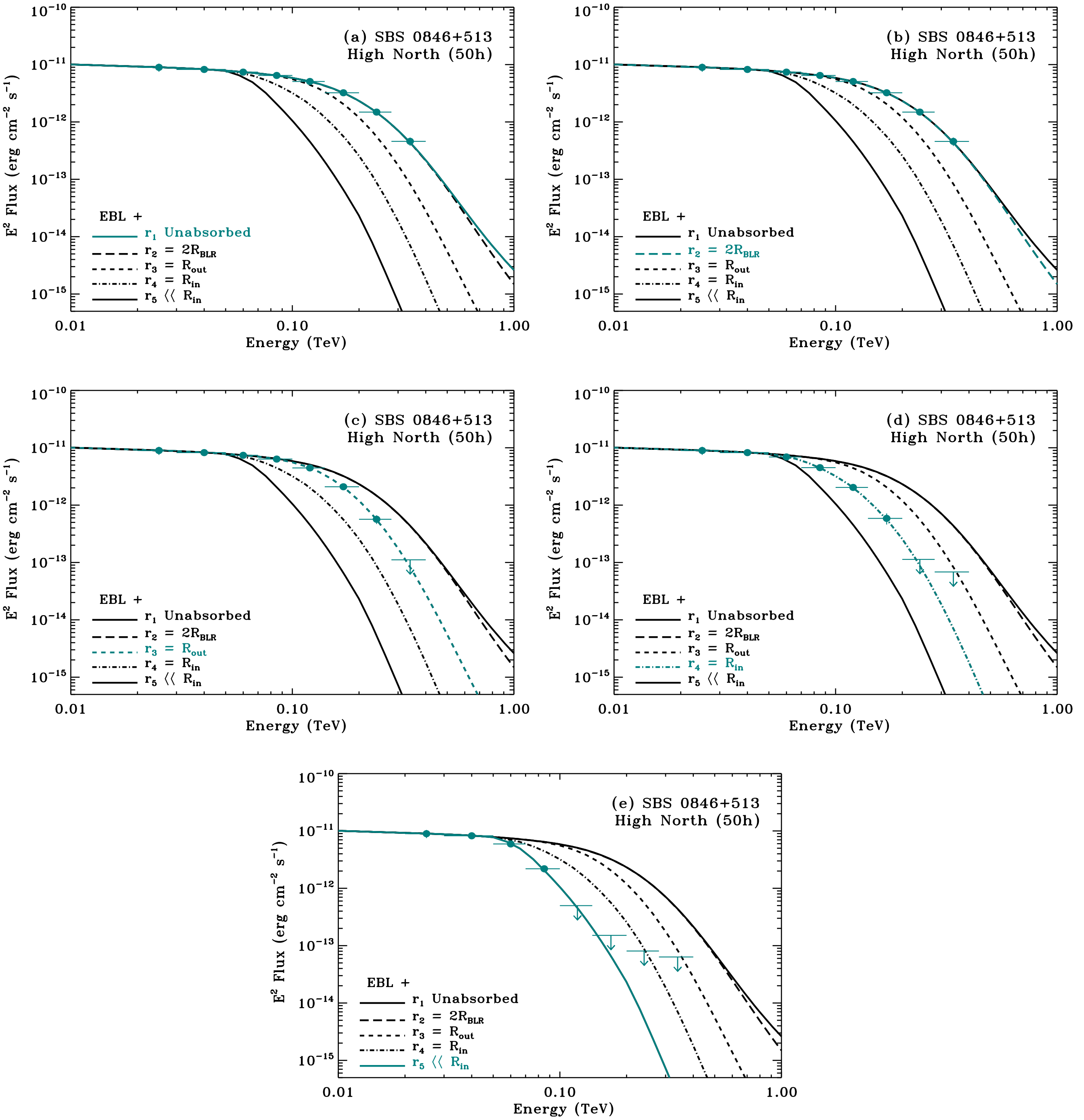

Figure 3. Input models for SBS 0846+513 in the high state, including both the BLR and the EBL contribution to absorption (black). The green thick line corresponds to the current input simulated model, while the filled green points represent the results of the simulations. The arrows represent the 95 per cent confidence level ULs. A colour version is available online.

4 SIMULATIONS

Our simulations were performed with the analysis package `ctools` (Knödlseder et al. 2016, v. 1.5.2)[2] and the public CTA instrument response files[3] (IRF, v. prod3b-v1). We considered only the instrumental background included in the IRFs (`CTAIrfBackground`) and no further contaminating astrophysical sources in the 5 deg field of view (FOV) we adopted for event extraction.

Following Romano et al. (2018), we simulated each source from the CTA site that provides the largest source elevation. The corresponding prod3b-v1 IRFs (reported in Table 3, Col. 3) were used for the simulations. We chose ‘the average’ IRFs for PMN J0948+0022 and PKS 1502+036, which are visible from both hemispheres and simulated the sources from the southern CTA site. For SBS 0846+513, which is only visible from the Northern hemisphere,

---

[2] http://cta.irap.omp.eu/ctools/.

[3] https://www.cta-observatory.org/science/cta-performance/.

Downloaded from https://academic.oup.com/mnras/article/494/1/411/5775321 by CNRS - ISTO user on 21 June 2022

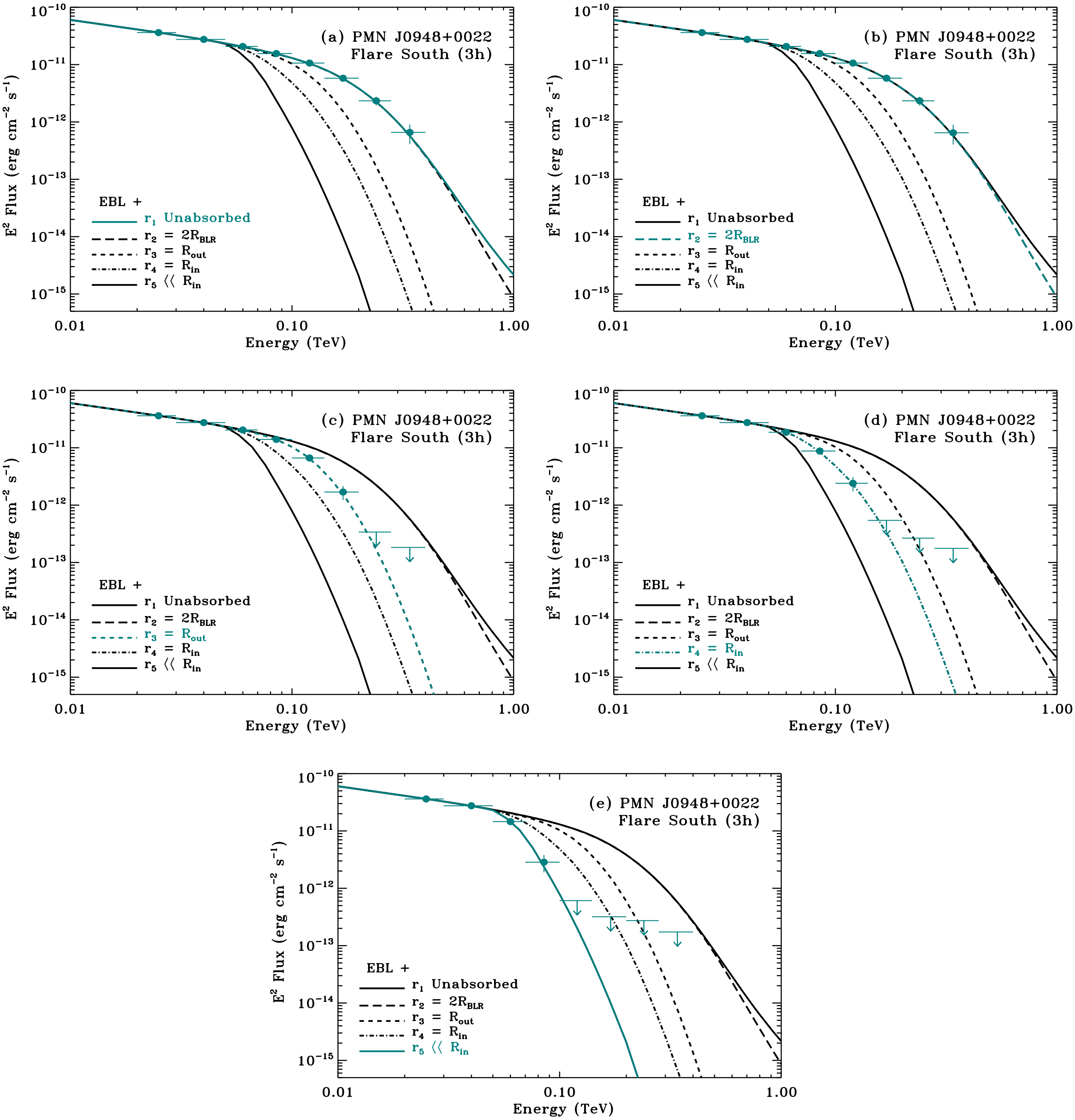

Figure 4. Same as Fig. 3 for PMN J0948+0022 in the flaring state.

Downloaded from https://academic.oup.com/mnras/article/494/1/411/5775321 by CNRS - ISTO user on 21 June 2022

where the geomagnetic field must be taken into account, we chose the azimuth-dependent IRF, corresponding to a pointing towards the magnetic North (see e.g. Hassan et al. 2017). We selected the exposures based on our findings in Romano et al. (2018), and we report them in Column 4 of Table 3. As detailed in Section 3, the input spectral model files for `ctools` were derived by extrapolating the best-fitting *Fermi* spectra (see Table 1) into the CTA energy range. We took into account both attenuation due to EBL and internal absorption.

We selected several energy ranges (20–30, 30–50, 50–70, 70–100, 100–140, 140–200, 200–280, 280–400 GeV) and extracted spectral points from the simulated CTA observations. In each band, we first used the task `ctobssim` to create event lists based on our input models, and then `ctlike` to fit a PL model $M_{\rm spectral}(E) = K_0(\frac{E}{E_0})^{-\Gamma}$ (where K_0 is the normalization, E_0 is the pivot energy, and Γ is the PL photon index) by using a maximum-likelihood model fitting. The normalization and photon index parameters were free to vary while the pivot energy was set to the geometric mean

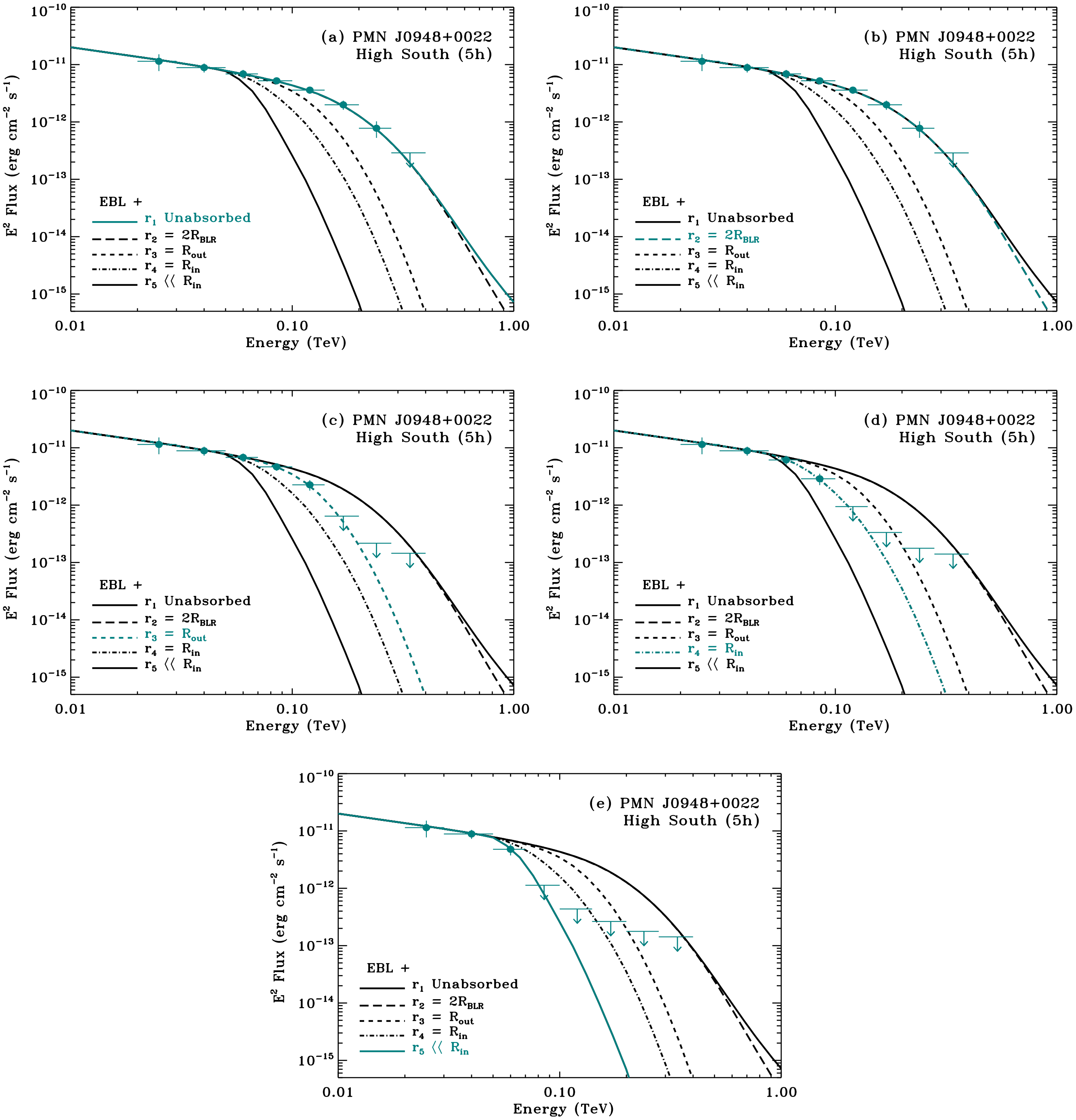

Figure 5. Same as Fig. 3 for PMN J0948+0022 in the high state.

of the boundaries of the energy bin. `ctlike` also calculates the test statistic (TS; Cash 1979; Mattox et al. 1996) of the maximum likelihood model fitting, which we used to assess the goodness of the detection in each band. We considered a detection to have a high significance when $\mathrm{TS} \geq 25$, a low significance when $10 \leq \mathrm{TS} < 25$, and not to be detected when $\mathrm{TS} < 10$.

We performed sets of $N = 100$ statistically independent realizations to reduce the impact of variations between individual realizations (see e.g. Knödlseder et al. 2016) and calculated the percentage of the detections for $\mathrm{TS} > 10$ and for $\mathrm{TS} > 25$, the mean TS value and its uncertainty, and the flux mean and its uncertainty. When the source was not detected, we calculated 95 per cent confidence level ULs on fluxes from the distribution of the simulated fluxes.

5 RESULTS

Figs 3–6 show the results of our simulations. For each source, in each panel, one of the five exemplary models considered is plotted in green (while the remaining four are plotted in black), so that the first panel represents the simulations for $r_1 \gg R_{\mathrm{out}}$ (i.e. the input spectrum unaffected by BLR absorption), the second

Downloaded from https://academic.oup.com/mnras/article/494/1/411/5775321 by CNRS - ISTO user on 21 June 2022

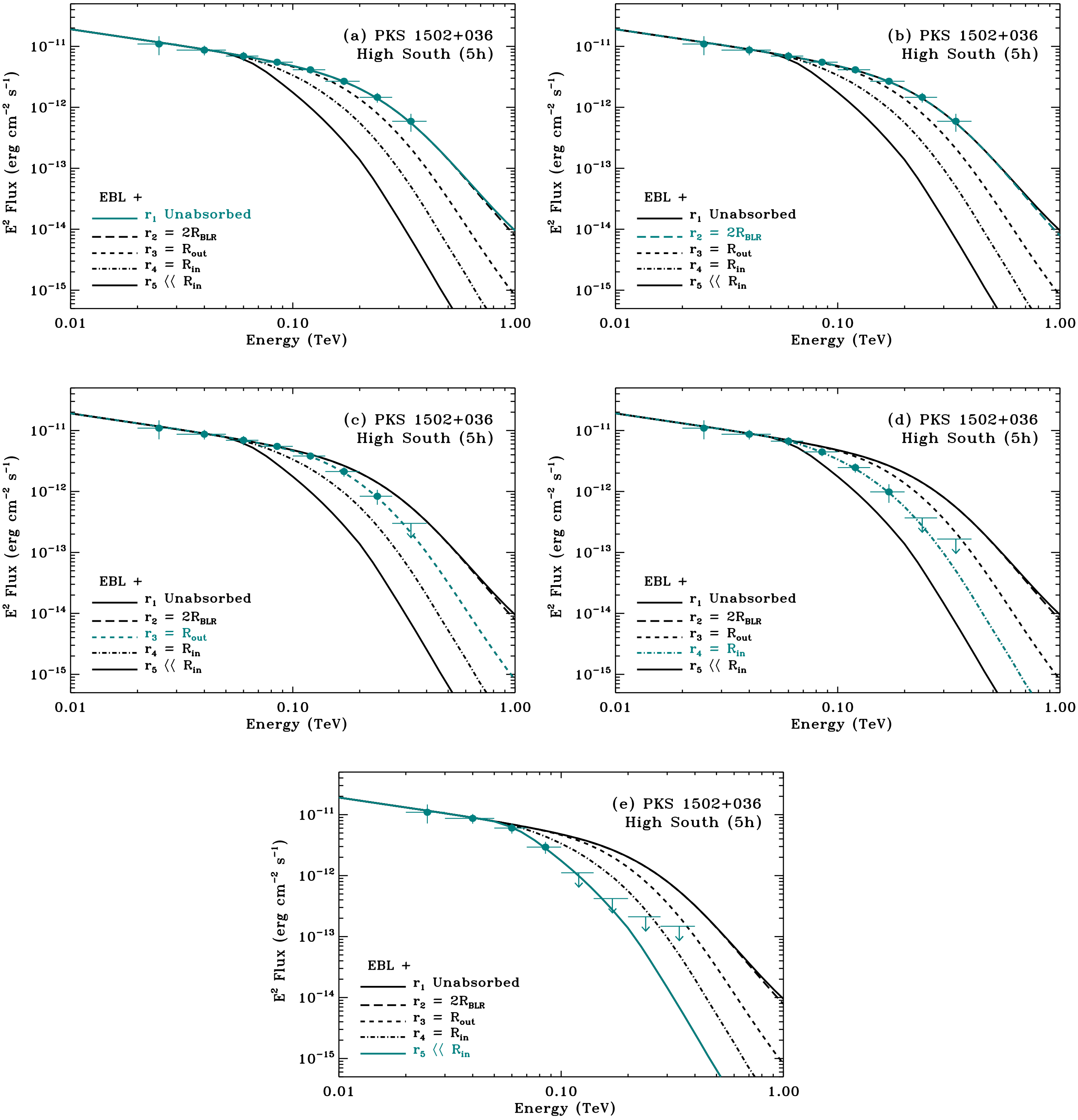

Figure 6. Same as Fig. 3 for PKS 1502+036 in the high state.

for $r_2 = 2\,R_{\rm BLR}$, the third for $r_3 = R_{\rm out}$, the fourth for $r_4 = R_{\rm in}$, and the fifth for $r_5 \ll R_{\rm in}$. The green points are the simulated fluxes for the current model, and the downward pointing arrows are ULs (95 per cent c.l.). Tables 4–7 report the details of the data points.

We can see that CTA observations will generally enable us to distinguish models with emitting radii within the BLR radius ($R_{\rm em} < R_{\rm in}$) from those with $R_{\rm em} \gtrsim R_{\rm out}$. This is particularly true for SBS 0846+513 in the high state and PMN J0948+0022 in flare, and for PKS 1502+036. As expected, for the case of PMN J0948+0022 this is more difficult, even in the high state considered here.

6 DISCUSSION

In Romano et al. (2018), we explored the prospects for observations with CTA of the largest sample of γ-NLS1s to date. For our simulations, we included both the extragalactic background light in the propagation of γ-rays and intrinsic absorption components. By adopting a simplified analytical description for the absorption of γ-rays within the source, a cut-off at 30 GeV ($\propto e^{-E/E_{\rm cut}}$, $E_{\rm cut} = 30$ GeV), we could select the best candidates for a prospective CTA detection: SBS 0846+513 (high state), PMN J0948+0022 (high state), and PKS 1502+036 (high and 'flare' states, see Section 2).

Downloaded from https://academic.oup.com/mnras/article/494/1/411/5775321 by CNRS - ISTO user on 21 June 2022

Table 4. Results of the simulations for the high state of SBS 0846+513.

Model	Energy range (GeV)	Det. c.l.[a] (TS > 10) (%)	Det. c.l.[a] (TS > 25) (%)	$\overline{\mathrm{TS}}_{\mathrm{sim}}$	E^2 flux[b] $\times 10^{-13}$ (erg cm^{-2} s^{-1})
r1	20–30	100.0	91.0	41.2 ± 11.5	89.6 ± 14.5
	30–50	100.0	100.0	126.3 ± 21.7	82.4 ± 7.7
	50–70	100.0	100.0	224.0 ± 26.9	74.0 ± 4.8
	70–100	100.0	100.0	433.4 ± 38.9	64.7 ± 3.1
	100–140	100.0	100.0	587.1 ± 44.6	50.8 ± 2.0
	140–200	100.0	100.0	624.6 ± 54.6	32.3 ± 1.5
	200–280	100.0	100.0	264.9 ± 34.3	14.9 ± 1.1
	280–400	100.0	99.0	59.8 ± 15.9	4.6 ± 0.8
r2	50–70	100.0	100.0	224.0 ± 26.9	74.0 ± 4.8
	70–100	100.0	100.0	433.4 ± 38.9	64.7 ± 3.1
	100–140	100.0	100.0	587.1 ± 44.6	50.8 ± 2.0
	140–200	100.0	100.0	624.6 ± 54.6	32.3 ± 1.5
	200–280	100.0	100.0	264.9 ± 34.3	14.9 ± 1.1
	280–400	100.0	99.0	59.5 ± 16.3	4.6 ± 0.8
r3	50–70	100.0	100.0	223.5 ± 27.0	73.9 ± 4.8
	70–100	100.0	100.0	417.6 ± 36.5	63.6 ± 3.0
	100–140	100.0	100.0	457.5 ± 39.2	44.5 ± 2.0
	140–200	100.0	100.0	292.7 ± 38.9	20.9 ± 1.5
	200–280	100.0	98.0	51.6 ± 14.3	5.7 ± 1.0
	280–400	14.8	0.0	5.1 ± 3.9	<1.1
r4	50–70	100.0	100.0	193.2 ± 24.6	69.2 ± 4.7
	70–100	100.0	100.0	215.1 ± 27.4	45.0 ± 2.9
	100–140	100.0	100.0	107.4 ± 20.3	20.4 ± 2.1
	140–200	99.0	62.0	30.3 ± 11.4	5.9 ± 1.3
	200–280	1.3	0.0	3.2 ± 2.8	<1.1
	280–400	0.0	0.0	1.8 ± 1.8	<0.7
r5	50–70	100.0	100.0	141.6 ± 21.5	59.4 ± 4.7
	70–100	100.0	100.0	60.4 ± 14.5	21.9 ± 3.0
	100–140	31.0	1.0	8.4 ± 5.4	<5.0
	140–200	0.0	0.0	2.6 ± 2.3	<1.5
	200–280	0.0	0.0	1.5 ± 1.4	<0.8
	280–400	0.0	0.0	1.7 ± 1.7	<0.6

[a] We consider a detection to have a high significance when TS $\geq$ 25 and a low significance when 10 $\leq$ TS $<$ 25. The source will not be considered detected for TS $<$ 10.

[b] ULs are calculated for 95 per cent confidence level for all cases where TS $<$ 10.

Table 5. Results of the simulations for the flare state of PMN J0948+0022.

Model	Energy range (GeV)	Det. c.l.[a] (TS > 10) (%)	Det. c.l.[a] (TS > 25) (%)	$\overline{\mathrm{TS}}_{\mathrm{sim}}$	E^2 flux[b] $\times 10^{-13}$ (erg cm^{-2} s^{-1})
r1	20–30	100.0	100.0	66.2 ± 17.2	361.8 ± 49.4
	30–50	100.0	100.0	169.8 ± 27.3	275.0 ± 23.2
	50–70	100.0	100.0	201.7 ± 29.9	207.3 ± 16.7
	70–100	100.0	100.0	282.1 ± 37.6	155.9 ± 11.7
	100–140	100.0	100.0	274.9 ± 36.9	106.4 ± 8.3
	140–200	100.0	100.0	198.0 ± 33.1	57.9 ± 5.4
	200–280	100.0	100.0	74.8 ± 21.3	23.4 ± 4.1
	280–400	71.7	15.2	15.8 ± 8.8	6.6 ± 2.4
r2	50–70	100.0	100.0	201.7 ± 29.9	207.3 ± 16.7
	70–100	100.0	100.0	282.1 ± 37.6	155.9 ± 11.7
	100–140	100.0	100.0	274.9 ± 36.9	106.4 ± 8.3
	140–200	100.0	100.0	198.0 ± 33.1	57.9 ± 5.4
	200–280	100.0	100.0	74.8 ± 21.3	23.4 ± 4.1
	280–400	70.7	13.1	15.6 ± 8.8	6.5 ± 2.4
r3	50–70	100.0	100.0	196.3 ± 30.4	204.5 ± 16.9
	70–100	100.0	100.0	231.9 ± 34.9	140.0 ± 11.9
	100–140	100.0	100.0	124.0 ± 23.6	66.4 ± 7.1
	140–200	94.0	60.0	27.5 ± 11.4	16.9 ± 4.6
	200–280	1.3	0.0	3.1 ± 2.7	<3.4
	280–400	0.0	0.0	1.8 ± 1.7	<1.8
r4	50–70	100.0	100.0	164.3 ± 23.4	186.4 ± 14.2
	70–100	100.0	100.0	104.7 ± 22.7	87.8 ± 10.5
	100–140	92.0	39.0	22.8 ± 9.6	24.0 ± 6.7
	140–200	4.9	0.0	3.6 ± 2.8	<5.4
	200–280	0.0	0.0	1.9 ± 1.9	<2.7
	280–400	0.0	0.0	1.7 ± 1.7	<1.8
r5	50–70	100.0	100.0	107.5 ± 21.2	145.5 ± 15.8
	70–100	78.0	18.0	17.2 ± 8.9	28.5 ± 9.6
	100–140	0.0	0.0	2.1 ± 2.1	<6.1
	140–200	0.0	0.0	1.5 ± 1.9	<3.2
	200–280	0.0	0.0	2.0 ± 1.9	<2.7
	280–400	0.0	0.0	1.7 ± 1.7	<1.7

[a] We consider a detection to have a high significance when TS $\geq$ 25 and a low significance when 10 $\leq$ TS $<$ 25. The source will not be considered detected for TS $<$ 10.

[b] ULs are calculated for 95 per cent confidence level for all cases where TS $<$ 10.

In this paper, we capitalized on this optimization of prospective CTA targets and, motivated by the evidence reported in Berton et al. (2016) that radio-loud NLS1s seem to be the low-mass tail of FSRQs, we adopted more realistic absorption models as proposed for the two FSRQ 3C 279 and PKS 1510−089 by Böttcher & Els (2016). In that work, this included, within the single-zone leptonic EC-BLR model scenario, a detailed treatment of γ–γ absorption in the radiation fields of the BLR as a function of the location of the γ-ray emission region with parameters inferred from the individual shape of the spectral energy distribution. For the purpose of this paper, the BLR parameters (radius and luminosity) were kept fixed based on the observational constraints on the accretion-disc and BLR luminosities of each of the three NLS1s we examined (Section 3).

Fig. 2 compares the input models (including both the BLR and the EBL contribution to absorption) of the simplified models of Romano et al. (2018), in blue (PL + EBL + BLR absorption) and red (PL + EBL), and the ones presented here. For SBS 0846+513 and PMN J0948+0022 the approximation adopted in Romano et al. (2018) was very conservative when compared with the new models, as the shape of the predicted spectrum was quite different and, in the case of absorbed models, considerably fainter for energies below 100 GeV. Also, since the new models diverge sufficiently only above ~50 GeV, and the CTA sensitivity[4] is particularly competitive with respect to *Fermi* in that energy range, especially for short time-scale phenomena (see Bulgarelli et al. 2015; Fioretti et al. 2015; Cherenkov Telescope Array Consortium et al. 2017), CTA is particularly well suited to disentangle these models.

We also note that our new models are still based on very conservative assumptions with respect to other models (see Tavecchio & Mazin 2009), first because of the factor of 3 in equation (2), which differs from, e.g. Ghisellini & Tavecchio (2008) but is consistent with Bentz et al. (2013); and second because of the assumed BLR geometry, a spherical homogeneous shell, which provides

---

[4] https://www.cta-observatory.org/science/cta-performance/#1525680063092-06388df6-d2af.

Downloaded from https://academic.oup.com/mnras/article/494/1/411/5775321 by CNRS - ISTO user on 21 June 2022

Table 6. Results of the simulations for the high state of PMN J0948+0022.

Model	Energy range (GeV)	Det. c.l.[a] (TS > 10) (%)	Det. c.l.[a] (TS > 25) (%)	$\overline{\mathrm{TS}_{\mathrm{sim}}}$	E^2 flux[b] $\times 10^{-13}$ (erg cm^{-2} s^{-1})
r1	20–30	69.0	9.0	14.0 ± 7.4	114.3 ± 37.2
	30–50	100.0	79.0	33.9 ± 10.9	88.6 ± 15.9
	50–70	100.0	94.0	43.5 ± 13.5	68.8 ± 12.0
	70–100	100.0	100.0	63.8 ± 16.0	52.2 ± 7.2
	100–140	100.0	100.0	65.2 ± 15.5	35.9 ± 4.9
	140–200	100.0	96.0	50.9 ± 16.4	19.9 ± 3.6
	200–280	80.0	23.0	18.8 ± 9.5	7.8 ± 2.5
	280–400	16.7	0.0	5.6 ± 4.7	<2.9
r2	50–70	100.0	94.0	43.5 ± 13.5	68.8 ± 12.0
	70–100	100.0	100.0	63.8 ± 16.0	52.2 ± 7.2
	100–140	100.0	100.0	65.2 ± 15.5	35.9 ± 4.9
	140–200	100.0	96.0	50.9 ± 16.4	19.9 ± 3.6
	200–280	80.0	23.0	18.8 ± 9.5	7.8 ± 2.5
	280–400	15.6	0.0	5.6 ± 4.6	<2.9
r3	50–70	100.0	93.0	42.5 ± 12.7	68.0 ± 11.4
	70–100	100.0	98.0	51.5 ± 13.1	46.5 ± 6.8
	100–140	99.0	61.0	29.3 ± 10.2	22.6 ± 4.7
	140–200	27.8	0.0	7.3 ± 5.5	<6.4
	200–280	1.8	0.0	2.2 ± 2.2	<2.2
	280–400	0.0	0.0	1.8 ± 1.7	<1.4
r4	50–70	100.0	83.0	35.3 ± 11.1	61.3 ± 11.2
	70–100	96.0	38.0	22.5 ± 8.1	28.8 ± 6.5
	100–140	20.4	0.0	6.2 ± 4.4	<9.4
	140–200	1.6	0.0	2.6 ± 2.3	<3.3
	200–280	2.0	0.0	1.7 ± 2.1	<1.8
	280–400	0.0	0.0	1.7 ± 1.7	<1.4
r5	50–70	96.0	43.0	23.2 ± 8.9	47.9 ± 10.5
	70–100	7.4	0.0	4.4 ± 3.4	<11.3
	100–140	0.0	0.0	1.7 ± 1.5	<4.4
	140–200	0.0	0.0	1.9 ± 1.9	<2.6
	200–280	2.1	0.0	1.7 ± 2.1	<1.8
	280–400	0.0	0.0	1.8 ± 1.7	<1.4

[a] We consider a detection to have a high significance when TS ≥ 25 and a low significance when 10 ≤ TS < 25. The source will not be considered detected for TS < 10.
[b] ULs are calculated for 95 per cent confidence level for all cases where TS < 10.

Table 7. Results of the simulations for the high state of PKS 1502+036.

Model	Energy range (GeV)	Det. c.l.[a] (TS > 10) (%)	Det. c.l.[a] (TS > 25) (%)	$\overline{\mathrm{TS}_{\mathrm{sim}}}$	E^2 flux[b] $\times 10^{-13}$ (erg cm^{-2} s^{-1})
r1	20–30	64.0	10.0	13.2 ± 7.1	109.4 ± 37.7
	30–50	100.0	80.0	32.7 ± 10.5	86.9 ± 15.8
	50–70	100.0	95.0	44.6 ± 13.8	69.3 ± 12.0
	70–100	100.0	100.0	70.7 ± 16.4	55.0 ± 7.0
	100–140	100.0	100.0	84.1 ± 17.7	41.3 ± 5.0
	140–200	100.0	100.0	84.3 ± 21.2	26.8 ± 3.6
	200–280	100.0	95.0	53.1 ± 16.6	14.6 ± 2.7
	280–400	83.0	33.0	20.0 ± 10.0	5.9 ± 1.9
r2	50–70	100.0	95.0	44.6 ± 13.8	69.3 ± 12.0
	70–100	100.0	100.0	70.7 ± 16.4	55.0 ± 7.0
	100–140	100.0	100.0	84.1 ± 17.7	41.3 ± 5.0
	140–200	100.0	100.0	84.3 ± 21.2	26.8 ± 3.6
	200–280	100.0	95.0	53.1 ± 16.6	14.6 ± 2.7
	280–400	83.0	33.0	20.0 ± 10.0	5.9 ± 1.9
r3	50–70	100.0	95.0	44.4 ± 13.7	69.2 ± 11.9
	70–100	100.0	100.0	70.9 ± 16.2	55.0 ± 6.9
	100–140	100.0	100.0	72.7 ± 17.2	38.2 ± 5.1
	140–200	100.0	98.0	57.0 ± 17.6	21.2 ± 3.7
	200–280	86.0	35.0	20.9 ± 9.1	8.4 ± 2.3
	280–400	19.3	0.0	6.0 ± 4.5	<3.0
r4	50–70	100.0	94.0	41.3 ± 11.6	66.9 ± 10.9
	70–100	100.0	97.0	47.5 ± 12.6	44.6 ± 6.6
	100–140	100.0	81.0	33.2 ± 9.9	24.7 ± 4.3
	140–200	75.0	15.0	15.9 ± 8.4	9.8 ± 3.3
	200–280	13.8	0.0	5.1 ± 4.0	<3.7
	280–400	0.0	0.0	2.4 ± 2.3	<1.7
r5	50–70	100.0	80.0	34.2 ± 11.2	60.3 ± 11.4
	70–100	98.0	40.0	23.1 ± 8.3	29.3 ± 6.5
	100–140	31.3	0.0	7.9 ± 4.9	<11.1
	140–200	6.2	0.0	3.6 ± 3.3	<4.2
	200–280	1.8	0.0	2.2 ± 2.2	<2.1
	280–400	0.0	0.0	1.8 ± 1.7	<1.5

[a] We consider a detection to have a high significance when TS ≥ 25 and a low significance when 10 ≤ TS < 25. The source will not be considered detected for TS < 10.
[b] ULs are calculated for 95 per cent confidence level for all cases where TS < 10.

the highest optical depth when compared with other geometries, for example a ring (see e.g. fig. 15 of Finke 2016). Also, as shown by Abdo et al. (2009a), any reasonable BLR geometry does not significantly affect the model results.

In principle, both the torus and the accretion disc could be considered as further sources of absorption. However, at energies $E \lesssim 400$ GeV, where NLS1s might plausibly be detected, the torus contribution to absorption is probably irrelevant, as only a detection at ∼ 1 TeV would probe a torus component (see Finke 2016, fig. 14). Similarly, the disc is only dominant for $r < 10^{16}$ cm (see Finke 2016, fig. 15).

In our modelling, we assumed that the curvature in the spectrum is exclusively due to γ–γ absorption, but we note that there could be additional curvature due to a break or curvature in the e$^-$ spectrum or to Klein–Nishina effect. Such intrinsic curvature could adversely affect their detectability in CTA observations.

In order to address this concern, we can take advantage of the extent of the CTA energy range to consider a comparison with the extrapolation of a log-parabolic (LP) model fit to the *Fermi* data. The LP model is described by

$$\frac{\mathrm{d}N}{\mathrm{d}E} = K_0 \left(\frac{E}{E_0}\right)^{-\alpha-\beta\ln(E/E_0)}, \qquad (5)$$

where K_0 is the normalization, E_0 is the pivot energy, α is the local spectral slope at $E = E_0$, and β the curvature. We drew the LP models for the three sources from the Fermi Large Area Telescope Fourth Source Catalog (The *Fermi*–LAT collaboration 2019), and renormalized to the integrated 100 MeV to 100 GeV flux as extrapolated by adopting the PL models detailed in Table 1. The renormalization was obtained by keeping E_0, α, and β fixed. Fig. 7 shows this comparison for the high states of SBS 0846+513, PMN J0948+0022, and PKS 1502+036, where the LP model is represented by a violet long-dashed curve. Even in this case, it will be fairly easy for CTA to distinguish among the models.

Our simulations, reported in Figs 3–6, show that for SBS 0846+513 and PKS 1502+036 in the high state and PMN J0948+0022 in flare it is possible for CTA to distinguish

Downloaded from https://academic.oup.com/mnras/article/494/1/411/5775321 by CNRS - ISTO user on 21 June 2022

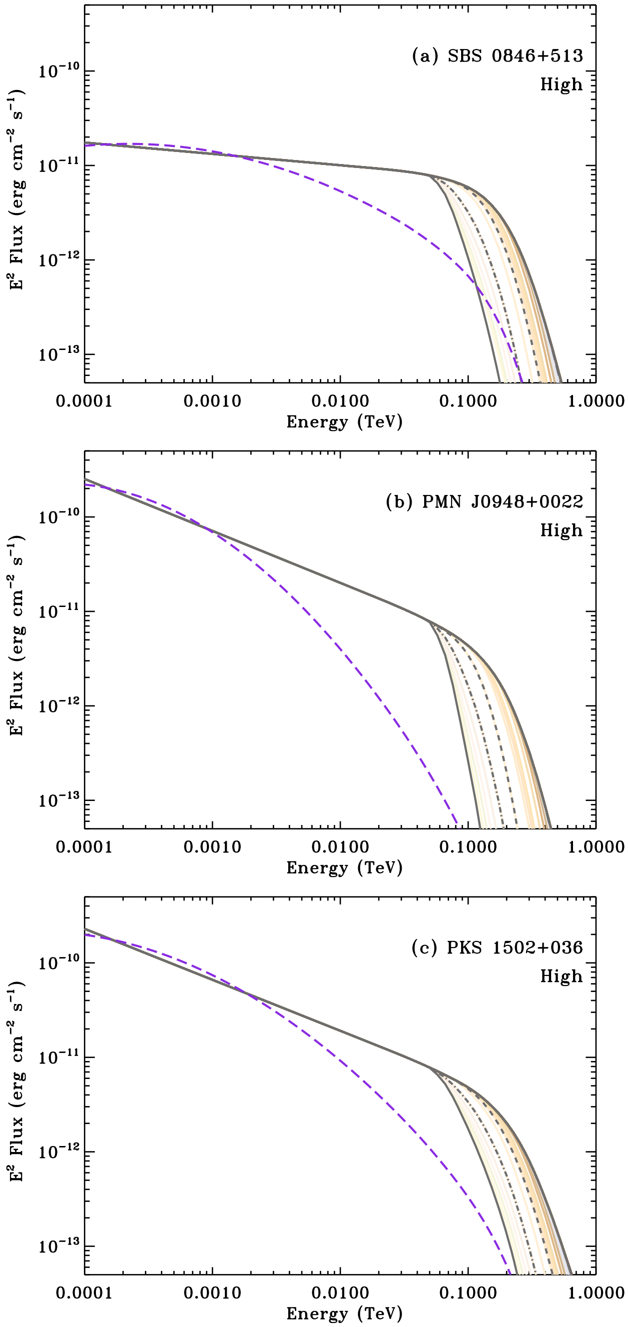

Figure 7. Comparison of the input models for our simulations and the extrapolation of the 4FGL log-parabola (violet long-dashed curve) fits scaled at the same Fermi flux. A colour version is available online.

among our models based on γ–γ absorption with emitting radii inside the BLR ($R_{\rm em} < R_{\rm in}$) from those with $R_{\rm em} \gtrsim R_{\rm out}$. In the case of low-synchrotron-peaked blazars (in particular, FSRQs), leptonic modelling of the SEDs typically requires a significant contribution of the BLR to the external radiation field for Compton up-scattering to produce the observed *Fermi*-LAT fluxes and spectra (e.g. Ghisellini et al. 2010; Böttcher et al. 2013). This, along with the rapid (sub-hour) variability observed in many FSRQs (e.g. Ackermann et al. 2016; Shukla et al. 2018), argues against a location of the γ-ray emission far beyond the BLR, at ≫pc scales in FSRQs. At the same time, at least for FSRQs with prominent accretion-disc and BLR emission, the same kind of BLR absorption constraints evaluated here for γ-NLS1s, precludes a location of the γ-ray emission region inside the BLR (e.g. Donea & Protheroe 2003; Reimer 2007; Liu, Bai & Ma 2008; Sitarek & Bednarek 2008; Böttcher & Els 2016). In the case of several observations, especially of FSRQs, this led to the conclusion that the most likely location is at $R_{\rm em} \sim R_{\rm out}$ (e.g. Barnacka et al. 2014; H.E.S.S. Collaboration 2019, 2020), although counter examples indicating a location of the γ-ray emission region at several pc from the central engine also exist (e.g. Agudo et al. 2011). Finally, it is also worth noting the instances in which location of γ-ray emission in the same source changes in different epochs (Foschini et al. 2008, 2011a; Ghisellini et al. 2013; Pacciani et al. 2014; Ahnen et al. 2015). The similarity of the non-thermal (likely jet-dominated) components of the SEDs of γ-NLS1s and FSRQs seems to suggest that similar processes (i.e. external-Compton dominated γ-ray emission) may be at work in both classes of sources (e.g. Abdo et al. 2009a; Berton et al. 2016; Arrieta-Lobo, Boisson & Zech 2017). Currently, seven FSRQs have been detected by IACTs (MAGIC Collaboration 2008; Aleksić et al. 2011; H.E.S.S. Collaboration 2013; Abeysekara et al. 2015; Ahnen et al. 2015; Sitarek et al. 2015; Cerruti et al. 2017; Mirzoyan 2017; Mukherjee & VERITAS Collaboration 2017; also see TeVCat[5] for further references). A significant detection of γ-NLS1 by CTA at $E \gtrsim 100$ GeV would then lead to similar conclusions about the location of the γ-ray emission region, i.e. near the outer edge of the BLR.

Looking at future perspectives, when the CTA data will be available, we sought to obtain a finer spectral binning by optimizing the energy resolution with a dynamical binning to further improve our chances of disentangling the competing models. The method is described in detail in Appendix A. Our results, obtained for the test case of PKS 1502+036 are shown in Fig. 8. As a comparison with a static energy binning (Section 4), the top panel of Fig. 8 summarizes and zooms in on the points in panels c,d, and e of Fig. 6. The middle panels were obtained with dynamic energy binning by ensuring a TS > 10 in each bin and an energy step of 10 (left) and 20 GeV (right). Similarly, the bottom panels were obtained with dynamic energy binning ensuring TS > 25 in each bin. This method will clearly improve our chances of discriminating between competing models while simultaneously providing a better chance to study in detail the curvature of the spectrum.

In conclusion, we also note that an important contribution in our ability to distinguish among competing models can be obtained by a carefully planned, and strictly simultaneous, multiwavelength campaign around high or flaring states in NLS1s. Indeed, the possible degeneracy within the VHE band can be lifted when optical–X-ray observations are used to constrain the electron distribution based on the shape of the synchrotron portion of the spectrum.

ACKNOWLEDGEMENTS

We thank J. Knödlseder and R. Terrier for helpful discussions, and M. Cerruti, S. Razzaque, and J. Biteau as internal CTA reviewer. PR and SV thank the staff at the Observatoire de Paris in Meudon, where part of the work was carried out, and Amos, for keeping them on schedule. We acknowledge financial contribution from the agreement ASI-INAFn. 2017-14-H.0. This research has made use of the NASA/IPAC Extragalactic Database (NED) which is operated by the Jet Propulsion Laboratory, California Institute

---

[5] http://tevcat.uchicago.edu/.

Downloaded from https://academic.oup.com/mnras/article/494/1/411/5775321 by CNRS - ISTO user on 21 June 2022

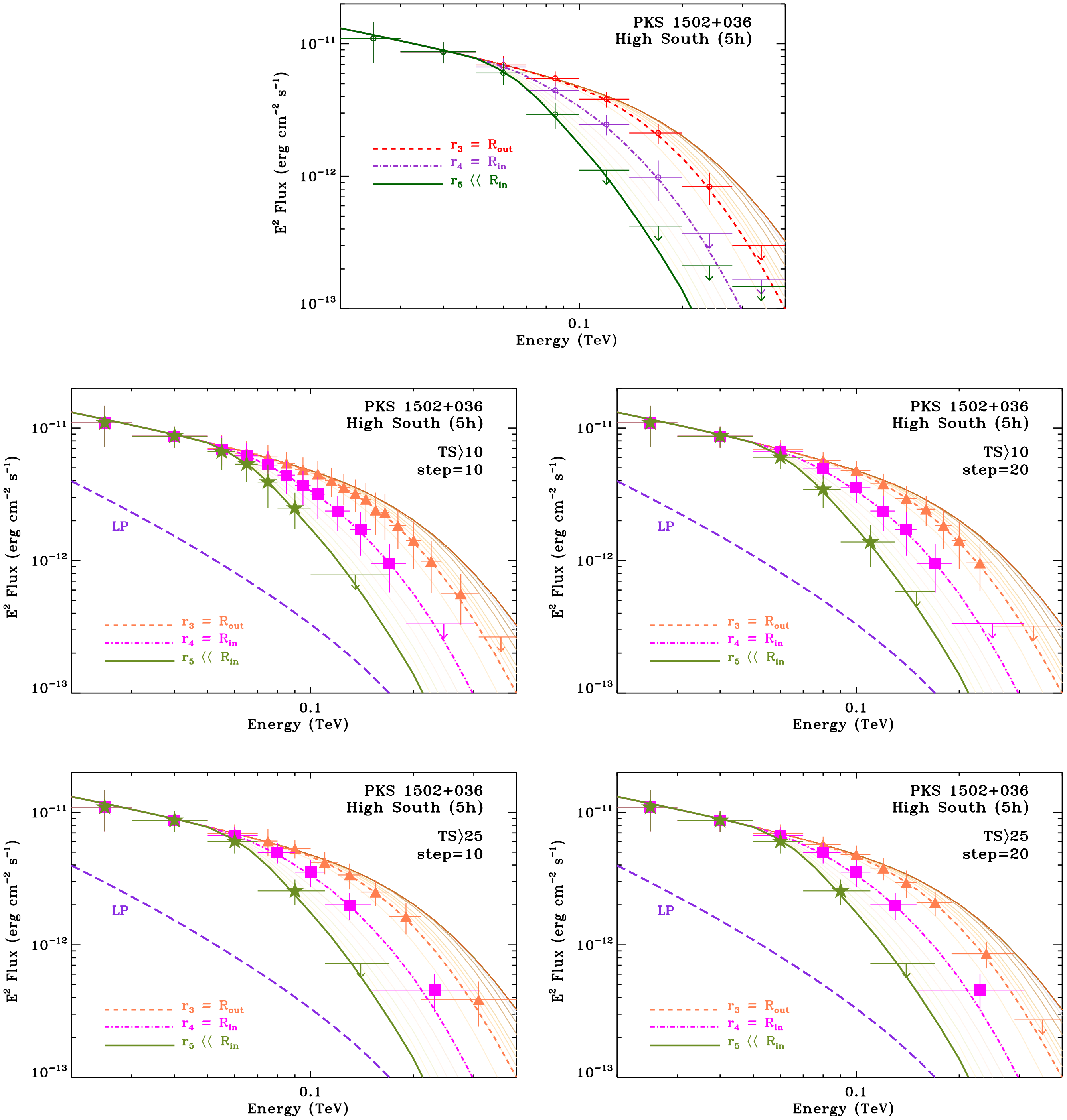

Figure 8. Example of dynamical binning. PKS 1502+036 in the high state. The top panel is a zoom of Fig. 6 (points in panels c, d, and e). The middle panels were obtained with dynamic energy binning by ensuring a TS > 10 in each bin and an energy step of 10 (left) and 20 GeV (right). The bottom panels were obtained with dynamic energy binning by ensuring a TS > 25 in each bin and an energy step of 10 (left) and 20 GeV (right). The violet long-dashed curve is the extrapolation of the 4FGL log-parabola fits scaled at the same Fermi flux. A colour version is available online.

of Technology, under contract with the National Aeronautics and Space Administration.

This research made use of `ctools`, a community-developed analysis package for Imaging Air Cherenkov Telescope data. ctools is based on `GammaLib`, a community-developed toolbox for the high-level analysis of astronomical gamma-ray data.

This research has made use of the CTA instrument response functions provided by the CTA Consortium and Observatory, see https://www.cta-observatory.org/science/cta-performance/ (version prod3b-v1) for more details.

We gratefully acknowledge financial support from the agencies and organizations listed here: http://www.cta-observatory.org/consortium_acknowledgments. This paper went through internal review by the CTA Consortium.

We also thank the anonymous referee for comments that helped improve the paper.

Downloaded from https://academic.oup.com/mnras/article/494/1/411/5775321 by CNRS - ISTO user on 21 June 2022

REFERENCES

Abdo A. A. et al., 2009a, ApJ, 699, 976

Abdo A. A. et al., 2009b, ApJ, 707, 727

Abeysekara A. U. et al., 2015, ApJ, 815, L22

Ackermann M. et al., 2016, ApJ, 824, L20

Agudo I. et al., 2011, ApJ, 735, L10

Ahnen M. L. et al., 2015, ApJ, 815, L23

Aleksić J. et al., 2011, ApJ, 730, L8

Arrieta-Lobo M., Boisson C., Zech A., 2017, FrASS, 4, 56

Barnacka A., Moderski R., Behera B., Brun P., Wagner S., 2014, A&A, 567, A113

Bentz M. C. et al., 2013, ApJ, 767, 149

Berton M. et al., 2016, A&A, 591, A98

Böttcher M., Els P., 2016, ApJ, 821, 102, Erratum: Böttcher M., Els P., 2018, ApJ, 869, 87

Böttcher M., Reimer A., Sweeney K., Prakash A., 2013, ApJ, 768, 54

Bulgarelli A. et al., 2015, in Borisov A. S. et al., eds, 34th International Cosmic Ray Conference (ICRC2015). SISSA, Trieste, PoS, 236, 763, https://pos.sissa.it/236/763/pdf

Cash W., 1979, ApJ, 228, 939

Cerruti M., Lenain J.-P., Prokoph H., H. E. S. S. Collaboration, 2017, 35th International Cosmic Ray Conference (ICRC2017). SISSA, Trieste, PoS, 301, 627, https://pos.sissa.it/301/627/pdf

Cherenkov Telescope Array Consortium, 2018, Science with the Cherenkov Telescope Array. World Scientific Publ. Co. Pte Ltd., Singapore

Cracco V., Ciroi S., Berton M., Di Mille F., Foschini L., La Mura G., Rafanelli P., 2016, MNRAS, 462, 1256

D'Ammando F. et al., 2015a, MNRAS, 446, 2456

D'Ammando F., Orienti M., Finke J., Larsson J., Giroletti M., Raiteri C., 2016a, Galaxies, 4, 11

D'Ammando F. et al., 2016b, MNRAS, 463, 4469

Domínguez A. et al., 2011, MNRAS, 410, 2556

Donea A.-C., Protheroe R. J., 2003, Astropart. Phys., 18, 377

Falcone A. D. et al., 2004, ApJ, 613, 710

Finke J. D., 2016, ApJ, 830, 94

Fioretti V., Bulgarelli A., Zoli A., Markoff S., Ribó M., Inoue S., Grandi P., De Cesare G., 2015, in Borisov A. S., et al., eds., 34th International Cosmic Ray Conference (ICRC2015). SISSA, Trieste, PoS, 236, 699, https://pos.sissa.it/236/699/pdf

Foschini L. et al., 2008, A&A, 484, L35

Foschini L., Maraschi L., Tavecchio F., Ghisellini G., Gliozzi M., Sambruna R. M., 2009, Adv. Space Res., 43, 889

Foschini L., Fermi/Lat Collaboration, Ghisellini G., Maraschi L., Tavecchio F., Angelakis E., 2010, in Maraschi L., Ghisellini G., Della Ceca R., Tavecchio F., eds, Accretion and Ejection in AGN: A Global View. Astron. Soc. Pac., San Francisco, 427, 243

Foschini L., Ghisellini G., Tavecchio F., Bonnoli G., Stamerra A., 2011a, 2011 Fermi Symposium Proceedings. eConf C110509, preprint (arXiv:1110.4471)

Foschini L. et al., 2011b, MNRAS, 413, 1671

Foschini L., 2012, Nuclei of Seyfert galaxies and QSOs - Central engine & conditions of star formation, SISSA, Trieste, PoS, 169, 10, https://pos.sissa.it/169/010/pdf

Foschini L. et al., 2015, A&A, 575, A13

Francis P. J., Hewett P. C., Foltz C. B., Chaffee F. H., Weymann R. J., Morris S. L., 1991, ApJ, 373, 465

Ghisellini G., Tavecchio F., 2008, MNRAS, 387, 1669

Ghisellini G., Tavecchio F., Foschini L., Ghirlanda G., Maraschi L., Celotti A., 2010, MNRAS, 402, 497

Ghisellini G., Tavecchio F., Foschini L., Bonnoli G., Tagliaferri G., 2013, MNRAS, 432, L66

Goodrich R. W., 1989, ApJ, 342, 224

H. E. S. S. Collaboration, 2013, A&A, 554, A107

H. E. S. S. Collaboration, 2014, A&A, 564, A9

H. E. S. S. Collaboration, 2019, A&A, 627, A159

H. E. S. S. Collaboration, 2020, A&A, 633, A162

Hassan T. et al., 2017, Astropart. Phys., 93, 76

Hofmann W., 2017a, The Messenger, 168, 21

Hofmann W., 2017b, in Aharonian F. A., Rieger F. M., eds, AIP Conf. Proc. Vol. 1792, 6th International Symposium on High Energy Gamma-Ray Astronomy. Heidelberg, p. 020014

Knödlseder J. et al., 2016, A&A, 593, A1

Komossa S., Voges W., Xu D., Mathur S., Adorf H.-M., Lemson G., Duschl W. J., Grupe D., 2006, AJ, 132, 531

Lähteenmäki A. et al., 2017, A&A, 603, A100

Liu H. T., Bai J. M., Ma L., 2008, ApJ, 688, 148

Lott B., Escande L., Larsson S., Ballet J., 2012, A&A, 544, A6

MAGIC Collaboration, 2008, Science, 320, 1752

Mattox J. R. et al., 1996, ApJ, 461, 396

Mirzoyan R., 2017, Astron. Telegram, 11061, 1

Mukherjee R., VERITAS Collaboration, 2017, Astron. Telegram, 11075, 1

Oshlack A. Y. K. N., Webster R. L., Whiting M. T., 2001, ApJ, 558, 578

Osterbrock D. E., Pogge R. W., 1985, ApJ, 297, 166

Pacciani L., Tavecchio F., Donnarumma I., Stamerra A., Carrasco L., Recillas E., Porras A., Uemura M., 2014, ApJ, 790, 45

Paliya V. S., Rajput B., Stalin C. S., Pandey S. B., 2016, ApJ, 819, 121

Peterson B. M. et al., 2004, ApJ, 613, 682

Reimer A., 2007, ApJ, 665, 1023

Romano P., Vercellone S., Foschini L., Tavecchio F., Landoni M., Knödlseder J., 2018, MNRAS, 481, 5046 (Paper I)

Shukla A. et al., 2018, ApJ, 854, L26

Sitarek J. et al., 2015, in Borisov A. S. et al., eds, 34th International Cosmic Ray Conference (ICRC2015). SISSA, Trieste, PoS, 236, 825, https://pos.sissa.it/236/825/

Sitarek J., Bednarek W., 2008, MNRAS, 391, 624

Tavecchio F., Mazin D., 2009, MNRAS, 392, L40

The Fermi-LAT collaboration, 2020, ApJS, 247, 33

Viswanath G., Stalin C. S., Rakshit S., Kurian K. S., Ujjwal K., Gudennavar S. B., Kartha S. S., 2019, ApJ, 881, L24

Yuan W., Zhou H. Y., Komossa S., Dong X. B., Wang T. G., Lu H. L., Bai J. M., 2008, ApJ, 685, 801

Zhou H.-Y., Wang T.-G., Dong X.-B., Zhou Y.-Y., Li C., 2003, ApJ, 584, 147

APPENDIX A: FINER SPECTRAL CHARACTERIZATION WITH OPTIMISATION OF THE ENERGY BINS VIA DYNAMICAL BINNING

In the following we consider the case of PKS 1502+036 in high state to propose an iterative method to optimise the choice of the energy bins for spectrum calculations. While this may seem a purely academic pursuit at this point, it may yield the necessary edge to better discriminate among competing models when the data from CTA will be available. Furthermore, adaptive binning is commonly used in high energy astrophysics (see Lott et al. 2012, for *Fermi* light curves, rather than spectra, as we did in this paper).

We start from the lowest energy boundary, E_0, and select a small increment in energy $\mathrm{d}E$ (or 'step'). We then perform a 'detection', i.e. we

(i) create an event list with `ctobssim` with energies between E_0 and $E_0 + \mathrm{d}E$, $[E_0, E_0 + dE]$;

(ii) perform a maximum likelihood model fitting with `ctlike`;

(iii) check if the source is detected above a certain TS threshold value, $\mathrm{TS} \gtrsim \mathrm{TS}_{\mathrm{thresh}}$.

(a) If the source is detected ($\mathrm{TS} \gtrsim \mathrm{TS}_{\mathrm{thresh}}$), then we repeat for the next bin, defined by a lower energy boundary $E_0 + \mathrm{d}E$ and the same energy increment, $[E_0 + \mathrm{d}E, E_0 + 2\,\mathrm{d}E]$.

(b) If the source is not detected we repeat in the energy bin $[E_0, E_0 + 2\,\mathrm{d}E]$, or $[E_0, E_0 + n\,\mathrm{d}E]$, with n large enough that $\mathrm{TS} \gtrsim \mathrm{TS}_{\mathrm{thresh}}$.

Downloaded from https://academic.oup.com/mnras/article/494/1/411/5775321 by CNRS - ISTO user on 21 June 2022

The procedure is repeated until the high energy boundary of the bin reaches a reasonable E_{max}, as defined by the highest detection obtained without a dynamical binning.

For our example (Fig. 8), we used the models $r_3 = R_{\mathrm{out}}$, $r_4 = R_{\mathrm{in}}$, and $r_5 \ll R_{\mathrm{in}}$ as input models. We selected $E_0 = 50$ GeV, since below this energy the models are virtually indistinguishable, and $E_{\mathrm{max}} = 400$ GeV. Also, as a compromise between speed of processing and achieving a fine resolution in the resulting spectrum, we adopted a step of dE = 10 GeV and dE = 20 GeV. For the last bin, we calculated the 95 per cent confidence level ULs on fluxes from the distribution of the simulated fluxes (see Section 4). We considered both cases of a high significance detection ($\mathrm{TS}_{\mathrm{thresh}} = 25$) and the low significance detection ($\mathrm{TS}_{\mathrm{thresh}} = 10$).

This paper has been typeset from a TEX/LATEX file prepared by the author.

Downloaded from https://academic.oup.com/mnras/article/494/1/411/5775321 by CNRS - ISTO user on 21 June 2022